ROYAL SOCIETY
OF CHEMISTRY

PAPER

Check for updates

Enhancement of crystalline quality and solar-blind photodetection characteristics of ε-Ga₂O₃ films by introducing Zn impurity†

Xuan Sun,[ab] Kewei Liu, ⓘ *[ab] Xing Chen,[ab] Yongxue Zhu, ⓘ [a] Zhen Cheng,[a] Jialin Yang,[a] Binghui Li,[ab] Lei Liu ⓘ [ab] and Dezhen Shen*[ab]

ε-Ga₂O₃ films with and without Zn impurity were epitaxially grown by metal organic chemical vapor deposition on a *c*-plane sapphire substrate, and were then face-to-face annealed in an oxygen atmosphere at 600 °C. The structural and photoelectric properties of the thin films were characterized and analyzed in detail. The Zn-doped ε-Ga₂O₃ photodetector exhibits an ultra-high specific detectivity of 1.7×10^{16} Jones, a very quick response speed of less than 40 ms, and an extremely high UV-visible rejection ratio of 2.0×10^8 at a 10 V bias. In addition, the temperature dependent photoresponse properties have been investigated from 30 °C to 190 °C. The compensation effect of Zn impurities and their suppression of oxygen vacancies, as well as the improvement of crystal quality, should be responsible for the excellent performance of the device. Our results provide a new idea and guidance for achieving high-performance solar-blind photodetectors based on Ga₂O₃.

Introduction

Solar-blind ultraviolet (UV) photodetectors have important applications in confidential communication, fire warning, environmental monitoring, and so on.[1–8] Owing to its ultra-wide bandgap and significant thermal and chemical stability, gallium oxide (Ga₂O₃) has attracted a lot of attention and has become one of the most potential and popular materials in the field of solar blind UV detection.[9–12] Ga₂O₃ has six different crystal structures, including α-, β-, γ-, δ-, ε-, and κ-Ga₂O₃.[14–17] Among them, the most stable crystal structure is β-Ga₂O₃,[18,19] whereas ε-Ga₂O₃ is the metastable phase second only to β-Ga₂O₃.[20,21] Compared to β-Ga₂O₃, ε-Ga₂O₃ has a similar wide bandgap (∼4.9 eV), higher lattice symmetry, lower anisotropic crystal structure, and lower growth temperature.[22–25] In recent years, research studies on solar-blind UV detectors based on ε-Ga₂O₃ thin films have begun to rise and are receiving increasing attention.[26–28] Although many efforts are being dedicated towards developing high-performance ε-Ga₂O₃ thin film

solar-blind detectors, it is still a big challenge to simultaneously achieve low dark current, high specific detectivity, high UV-visible rejection ratio and quick response speed. The presence of a great number of oxygen vacancies should be the main cause of the above problems, as they not only act as donors providing free electrons, but also cause inter-band absorption, leading to visible light response. Thermal annealing in an oxygen atmosphere is a common route to passivate the oxygen vacancy defects in ε-Ga₂O₃.[30] However, the metastable nature of ε-Ga₂O₃ makes it difficult to completely suppress the adverse effects of oxygen vacancy defects on its photodetection performance through a simple high-temperature oxygen annealing process.

Owing to the similar ionic radii of Ga³⁺ (0.062 nm) and Zn²⁺ (0.074 nm), Zn alloying/doping has been widely used to improve the performance of Ga₂O₃,[31–35] and some results show that the oxygen vacancy defects can be significantly suppressed by introducing Zn into Ga₂O₃.[36,37] However, most previously studies have focused on the most stable β-Ga₂O₃, while relatively few studies have been conducted on other metastable phases;[38,39] in particular, Zn-doped ε-Ga₂O₃ has still not been reported. In this work, oxygen-vacancy-free ε-Ga₂O₃ film was epitaxially grown on a *c*-sapphire substrate using metal organic chemical vapor deposition (MOCVD) by introducing 6.34 at% Zn and face-to-face post-annealing in oxygen. In addition to the suppression of oxygen vacancies and the enhancement of the crystalline quality, the compensation effect of Zn impurities in ε-Ga₂O₃ films could contribute to the excellent performance of

---
[a] State Key Laboratory of Luminescence and Applications, Changchun Institute of Optics, Fine Mechanics and Physics, Chinese Academy of Sciences, No. 3888 Dongnanhu Road, Changchun, 130033, People's Republic of China. E-mail: liukw@ciomp.ac.cn, shendz@ciomp.ac.cn

[b] Center of Materials Science and Optoelectronics Engineering, University of the Chinese Academy of Sciences, Beijing 100049, People's Republic of China

† Electronic supplementary information (ESI) available: SEM, XPS, EDS, time-dependent photocurrent characteristics. See DOI: https://doi.org/10.1039/d3tc03599a

118 | *J. Mater. Chem. C,* 2024, **12**, 118–124

This journal is © The Royal Society of Chemistry 2024

its photodetector, which exhibits an ultra-low dark current of 0.75 pA, an ultra-high specific detectivity of 1.7×10^{16} Jones, and an extremely high rejection ratio of 2.0×10^8 at 10 V bias.

Experimental section

The ε-Ga$_2$O$_3$ epitaxial films with and without Zn doping were prepared by MOCVD on a *c*-plane sapphire substrate. We used diethylzinc (DEZn), triethylgallium (TEGa) and 5N oxygen as precursors of zinc, gallium and oxygen, respectively, and high-purity nitrogen gas was chosen as the carrier gas. The growth temperature and chamber pressure were respectively set to 680 °C and 980 Pa during the film growth with a growth rate of ∼90 nm min^{-1}. After that, the films were face-to-face annealed in oxygen for 120 min at a temperature of 600 °C. The crystal structure was studied using a Bruker D8GADDS X-ray diffractometer (XRD) with the radiation source of Cu Kα ($\lambda = 0.154$ nm). Scanning electron microscopy (SEM) (HITACHI S-4800) and UV-3101PC scanning spectrophotometry were used to investigate the morphological properties and the optical properties of the samples, respectively. The composition of the film was evaluated by X-ray energy dispersive spectroscopy (EDS) (GENESIS 2000 XMS60S). X-ray photoelectron spectroscopy (XPS) was used to measure the elements and chemical states of the films.

To further explore the photodetection functions of the pure ε-Ga$_2$O$_3$ and the Zn-doped ε-Ga$_2$O$_3$ films, we prepared Au interdigital electrodes on them using photolithography and lift-off processes to form metal–semiconductor–metal (MSM) photodetectors. A semiconductor device analyzer (Agilent B1500A) was used to test the current–voltage (*I–V*) characteristic curves and time-dependent photocurrent (*I–t*) curves. A monochromator was used to test the photoresponse of the detectors, and the source of light was a 200 W UV-enhanced Xe lamp.

Results and discussion

First, we characterized the ε-Ga$_2$O$_3$ films with and without Zn by XRD, and the result is shown in Fig. 1. Three sharp diffraction peaks at 19.22°, 38.93° and 59.93° can be indexed to the (002), (004) and (006) crystal planes of ε-Ga$_2$O$_3$, respectively

(JCPDS no. 01-082-3196). After the introduction of Zn impurities into the ε-Ga$_2$O$_3$ film, no additional diffraction peaks were observed, indicating that no new phases were generated. In addition, since Zn and Ga have similar ionic radii, the introduction of Zn does not cause obvious shift of XRD diffraction peaks of ε-Ga$_2$O$_3$ films. To further investigate the crystalline quality of ε-Ga$_2$O$_3$ films with and without Zn, as shown in Fig. 1(b), high resolution XRD measurements have been performed. The full width at half maximum (FWHM) of the (004) peak of the XRD rocking curve was estimated to be 0.7° and 0.57° for the ε-Ga$_2$O$_3$ films without and with Zn, respectively. ε-Ga$_2$O$_3$ is the metastable structure, so the introduction of impurities could reduce the stress, dislocations and grain boundaries in the films and in turn improve their stability and crystallization quality. This can be used to explain the narrowing of the FWHM of the XRD rocking curve after the introduction of Zn into ε-Ga$_2$O$_3$. Moreover, the Zn content was estimated to be 6.34 at% and the thickness of both two films is around 150 nm, as shown in Fig. S1 (ESI†) and Fig. S2 (ESI†), respectively.

Fig. 1(c) presents the optical transmission properties of the films. In the visible region, both the samples show greater than 85% of the average transmittance, and a sharp absorption edge can be observed at ∼250 nm. The relationship between $(\alpha h\nu)^2$ and photon energy ($h\nu$) is plotted (see the inset of Fig. 1c), where α is the absorption coefficient. The optical bandgap (E_g) of ε-Ga$_2$O$_3$ film and Zn-doped ε-Ga$_2$O$_3$ film can be determined to be 5.22 eV and 5.12 eV, respectively.

To analyze the chemical bond status of the samples, as shown in Fig. S3 (ESI†) and Fig. 2, XPS characterization has been performed on two films. Fig. 2(a) exhibits the high-resolution Ga 2p core-level spectra of the samples, and the peaks at 1117.4 eV and 1144.2 eV can be attributed to Ga 2p$_{3/2}$ and Ga 2p$_{1/2}$, respectively.[30,42,43] After introducing Zn impurities, the Ga 2p$_{3/2}$ and Ga 2p$_{1/2}$ peaks did not shift, but they widened and weakened in intensity. This may be due to the substitution impurities changing the original state of the Ga atoms in the lattice. The observed spin–orbit splitting is ∼26.8 eV, which is very much in line with the previously reported ε-Ga$_2$O$_3$.[44] Fig. 2(b) shows the high-resolution Zn 2p core-level spectrum of a Zn-doped ε-Ga$_2$O$_3$ film. The Zn 2p$_{3/2}$
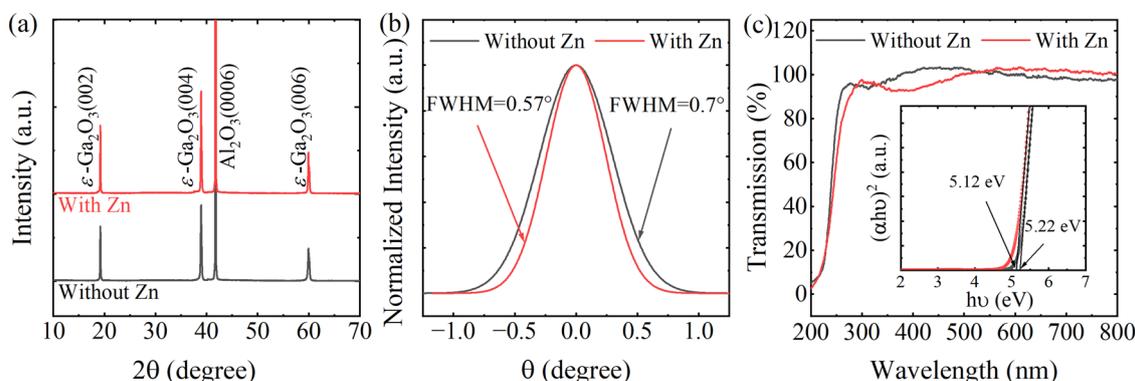

Fig. 1 (a) XRD patterns, (b) normalized XRD rocking curves of (004) plane and (c) optical transmission spectra of ε-Ga$_2$O$_3$ films with and without Zn.

This journal is © The Royal Society of Chemistry 2024

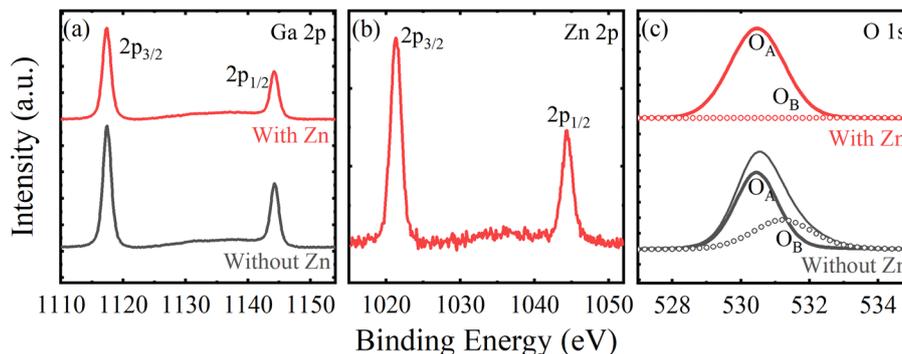*J. Mater. Chem. C*, 2024, **12**, 118–124 | **119**

Fig. 2 High-resolution XPS core-level spectra of (a) Ga 2p, (b) Zn 2p and (c) O 1s of the films.

and Zn $2p_{1/2}$ peaks can be obviously observed at 1021.3 and 1044.2 eV, respectively, indicating that Zn impurities have entered the crystal lattice well and participated in chemical bonding.[45] To explore the state of O atoms in the lattice, the high-resolution O 1s core level spectra for the films are shown in Fig. 2(c). The peak with lower binding energy (O_A) should be related to lattice oxygen (O^{2-}), and the peak with higher binding energy (O_B) corresponds to oxygen vacancies.[22,46,47] As we can see, the O_B peak of pure ε-Ga$_2$O$_3$ film is more pronounced, and tends to disappear after the introduction of Zn, indicating that the introduction of Zn inhibits the generation of oxygen vacancies.

Fig. 3(a) gives the I–V characteristics of the photodetectors based on ε-Ga$_2$O$_3$ films with and without Zn in the dark and under 254 nm (680 μW cm^{-2}) illumination. Clearly, the introduction of Zn could decrease the dark current and increase the light current at the same time. At 10 V, Zn-doped ε-Ga$_2$O$_3$ device has a low dark current of only 0.75 pA.

The photoresponse spectra of devices under 10 V bias are shown in Fig. 3(b). After the introduction of Zn impurities, the peak responsivity (R_{peak}) at ~250 nm significantly increased from 0.13 A W^{-1} to 118.7 A W^{-1}. And the UV-visible rejection ratio ($R_{peak}/R_{500\ nm}$) of a pure ε-Ga$_2$O$_3$ photodetector is only 5.9×10^3, while that of the Zn-doped device can reach as high as 2.0×10^8, indicating the excellent wavelength selectivity. Thanks to low dark current the high responsivity, the specific detectivity (D^*) of the Zn-doped ε-Ga$_2$O$_3$ photodetector is

calculated to be as high as 1.7×10^{16} cm Hz$^{1/2}$ W^{-1} (Jones) using the following formula:

$$D^* = \frac{R}{\sqrt{2qI_{dark}/S}} \qquad (1)$$

where R is the responsivity, S is the effective area of the device, I_{dark} is the current in dark and q is the free electron charge of 1.6×10^{-19} C.

Fig. 3(c) presents the I–t curves of solar-blind UV photodetectors at 10 V bias voltage under 254 nm light with an optical power density of 650 μW cm^{-2}. Both devices have excellent repeatability and stability. Notably, after the introduction of Zn impurities, the on/off current ratio increases from 4.8×10^2 to 4.9×10^8. Moreover, after switching off the light, the current of the Zn-doped ε-Ga$_2$O$_3$ solar-blind UV photodetector could completely recover to its initial dark state within 20 s, which is much better than that of the most early reported solar-blind UV photodetectors.[13,15,49–51]

The normalized transient photoresponse of the photodetector measured using an LED (255 nm) light source with different modulation frequencies of 0.1, 1, 10 and 100 Hz are shown in Fig. 4. With the increase in the modulation frequency, the photoresponse gradually decreases. The result shows that even at a high frequency of 100 Hz, the device can maintain high resolution and photoresponse over multiple cycles, confirming fast and reliable photo-switching. Moreover, 10–90% rise/decay
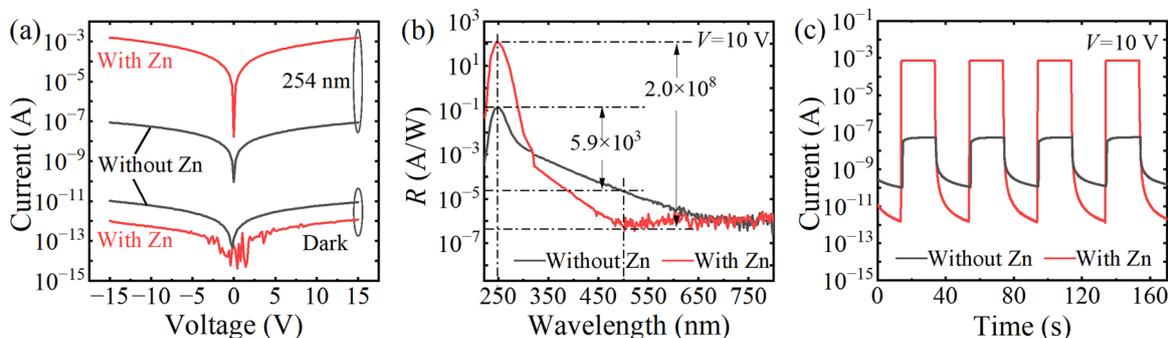

Fig. 3 (a) I–V curves, (b) the response spectra, and (c) I–t curves of the devices.

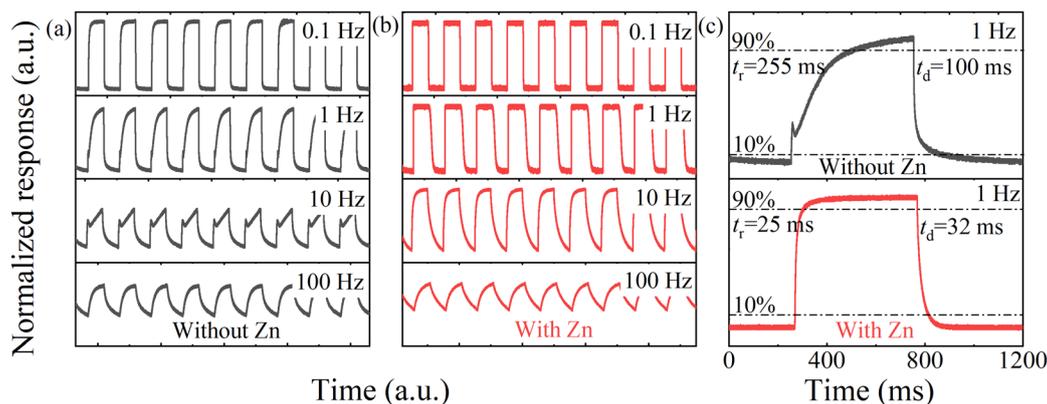**120** | J. Mater. Chem. C, 2024, **12**, 118–124

This journal is © The Royal Society of Chemistry 2024

Fig. 4 The transient photoresponse with different frequencies of the pure (a) and Zn-doped (b) ε-Ga$_2$O$_3$ devices; and (c) The transient photoresponse of the devices with frequencies of 1 Hz.

times (t_r/t_d) of the pure and Zn-doped ε-Ga$_2$O$_3$ devices can be estimated to be 255 ms/100 ms and 25 ms/32 ms, respectively.

To further investigate the effect of Zn on the properties of ε-Ga$_2$O$_3$, the temperature dependent electronic and optoelectronic characteristics of ε-Ga$_2$O$_3$ devices without and with Zn have been tested and investigated at different temperatures. With increasing the temperature from 30 °C to 190 °C, the dark current of pure ε-Ga$_2$O$_3$ detector increases from 5 pA to 0.2 nA at 10 V, as shown in Fig. 5(a), and an exponential relationship between dark current and temperature can be observed due to thermal ionization of donor defects.[52,53] As for the Zn-doped device, its dark current does not change much below 90 °C, but significantly increases with increasing temperature above 100 °C. This phenomenon should be associated with compensation effect and thermal ionization process of Zn impurities. Based on the current under 254 nm light illumination (650 μW cm^{-2}) in Fig. 5(a), the responsivity of the devices at different temperatures has been calculated as shown in Fig. 5(b), and the Zn-doped device shows obvious

photoconductive gain, while the pure ε-Ga$_2$O$_3$ detector has lower quantum efficiency. Moreover, the responsivity for the pure ε-Ga$_2$O$_3$ photodetector only undergoes minor change at 10 V with the increase of temperature, but the Zn-doped device shows a significant decrease.

To better understand the mechanism of the very different photoelectric characteristics of the two devices, the I–t curves were measured at 10 V bias voltage under various temperatures (see Fig. 5(c) and (d)). Clearly, with increasing the temperature, the response speed of Zn-doped detector increases significantly, while pure ε-Ga$_2$O$_3$ device gradually slows down. In addition, the decay curves of ε-Ga$_2$O$_3$ detectors with and without Zn can be well fitted to mono- and bi-exponential functions, respectively (see Fig. S4, ESI†). The mono- (eqn (2)) and bi-exponential (eqn (3)) decay equation are given below:

$$I(t) = I_0 + A_1 e^{\frac{-t}{\tau_1}} \quad (2)$$

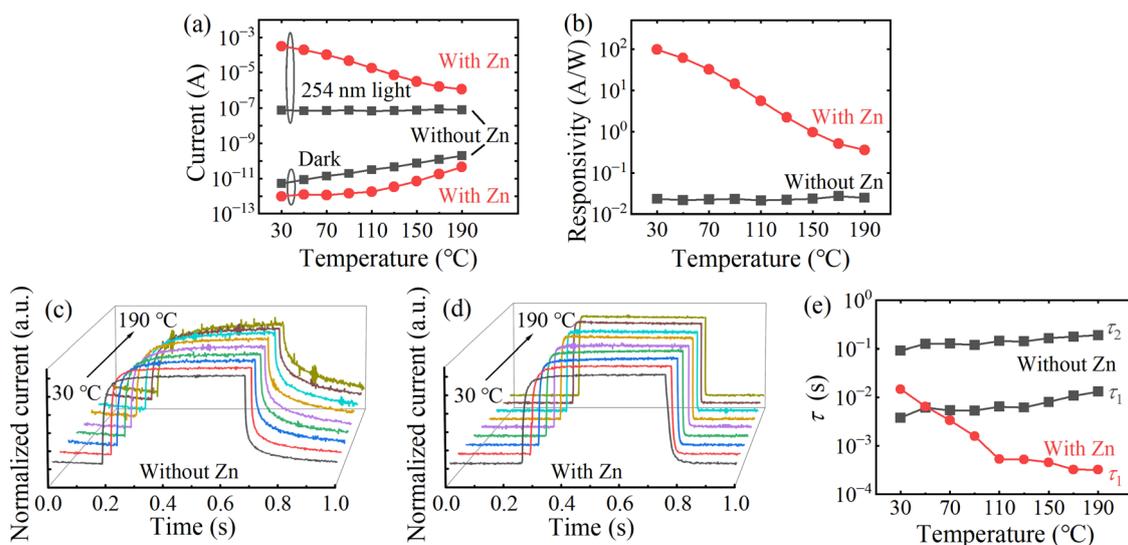$$I(t) = I_0 + A_1 e^{\frac{-t}{\tau_1}} + A_2 e^{\frac{-t}{\tau_2}} \quad (3)$$

Fig. 5 (a) The current and (b) responsivity as functions of operating temperature of the devices; The normalized transient photoresponse at different temperatures of the (c) pure and (d) Zn-doped ε-Ga$_2$O$_3$ devices; and (e) relaxation time constants as a function of operating temperature of the devices.

Table 1 Performance comparison of various solar-blind photodetectors based on ε-Ga$_2$O$_3$ films

Materials	Voltage (V)	UV-vis rejection ratio	Detectivity (Jones)	Response time t_r/t_d (s)	Ref.
ε-Ga$_2$O$_3$	6	—	4.2×10^{14}	—/0.1	13
ε-Ga$_2$O$_3$	6	1.2×10^5	1.2×10^{15}	—	29
ε-Ga$_2$O$_3$	5	6×10^3	1.2×10^{13}	7.6/5.2	40
ε-Ga$_2$O$_3$	5	1.8×10^7	9.13×10^{14}	0.05/0.09	30
ε-Ga$_2$O$_3$	5	1.3×10^4	1.67×10^{13}	0.62/0.33	41
ε-Ga$_2$O$_3$	5	—	4.37×10^{14}	1.38/0.14	42
ε-Ga$_2$O$_3$	2	—	2.49×10^{11}	—	44
ε-Ga$_2$O$_3$: Sn	20	—	—	0.41/0.16	48
ε-Ga$_2$O$_3$: Mg	5	—	2.85×10^{12}	1.6/5.4	49
ε-Ga$_2$O$_3$: Al	5	—	1.23×10^{13}	2.09/0.49	42
ε-Ga$_2$O$_3$	10	5.9×10^3	7.3×10^{12}	0.225/0.1	This work
Zn-doped ε-Ga$_2$O$_3$	10	2.0×10^8	1.7×10^{16}	0.025/0.032	This work

where I_0 is the steady-state current, t is the time, τ_1 and τ_2 are the relaxation time constants, and A_1 and A_2 are constants. For the pure ε-Ga$_2$O$_3$ detectors, the decay time consists of two components (fast and slow): the fast response component is caused by the rapid change in the carrier concentration after switching off the light, and the slow response component should be associated with carrier trapping effect of oxygen vacancy defects in the film. After the introduction of Zn, oxygen vacancy defects almost completely disappear, so the slow response component of the decay time of Zn-doped detector has been eliminated, and the lifetime of the carriers trapped at Zn-related defects is relatively short. The relaxation time constants as a function of temperature are plotted in Fig. 5(e) for two devices. According to the previous reports, the photoconductive gain (G) can be calculated using the following formula:

$$G = \frac{\tau \mu V}{L^2} \tag{4}$$

where τ is the lifetime of carriers, V is the applied voltage, μ is the carrier mobility and L is the interelectrode spacing. It is obvious that the gain is proportional to the carrier lifetime and mobility. However, in this work, the Zn-doped device has a shorter carrier lifetime than the undoped device but has much higher responsivity and gain. This can be explained by the higher crystalline quality of Zn-doped ε-Ga$_2$O$_3$, which in turn has a higher mobility of carriers. Additionally, in the Zn-doped ε-Ga$_2$O$_3$ device, as the temperature rises, the photogenerated holes trapped at Zn-related defects are more likely to escape and recombine with electrons, thereby shortening the carrier lifetime (Fig. 5(e), red dot line). Meanwhile, due to the enhanced scattering, the mobility of electrons also decreases with increasing temperature. The above mechanism can be used to explain that the responsivity and gain of the Zn-doped device decreases significantly with the increase of temperature. As for the pure ε-Ga$_2$O$_3$ detector, with the temperature rising from 30 °C to 190 °C, the higher barrier makes it difficult for the holes trapped by oxygen vacancies to escape and recombine with electrons. At the same time, the relatively poor crystal quality of the pure ε-Ga$_2$O$_3$ film and the enhancement of scattering caused by increasing temperature led to lower carrier mobility, lower recombination probability of trapped holes,

and a slow increase in its lifetime with increasing temperature (Fig. 5(e), black square line).

Table 1 exhibits the comparison between our Zn-doped ε-Ga$_2$O$_3$ device and some reported ε-Ga$_2$O$_3$ thin film based solar-blind photodetectors. It is clear that our device has excellent overall performance. The superior photodetection performance of our device indicates that ε-Ga$_2$O$_3$ films doped/alloyed with Zn have great potential in practical applications of solar-blind photodetectors.

Conclusions

In a word, pure and 6.34 at% Zn-doped ε-Ga$_2$O$_3$ films were epitaxially grown by MOCVD on c-plane sapphire substrates, followed by face-to-face annealing in an oxygen atmosphere at 600 °C. It is obvious that the introduction of Zn can greatly improve the solar-blind UV detection performance of ε-Ga$_2$O$_3$ films. At room temperature, a low dark current of 0.75 pA, a high $D^\star$ of 1.7×10^{16} Jones, and a large UV-visible rejection ratio of 2.0×10^8 at 10 V bias have been demonstrated for the Zn-doped detector. Moreover, a fast response speed (t_r = 25 ms, t_d = 32 ms) can be also observed and the current can attenuate by eight orders of magnitude and fully recover to the dark current state within 20 s after switching off the 254 nm light (650 μW cm^{-2}). The temperature dependent photoelectronic characteristics of both pure and Zn-doped ε-Ga$_2$O$_3$ suggested that the excellent performance of our Zn-doped ε-Ga$_2$O$_3$ film device can be attributed to the introduction of Zn impurities, which improves the crystal quality and stability of the ε-Ga$_2$O$_3$ metastable structure and inhibits the formation of oxygen vacancies. Our results provide a new idea for the realization of Ga$_2$O$_3$-based high-performance solar-blind photodetectors.

Author contributions

The manuscript was written through contributions of all authors. All authors have given approval to the final version of the manuscript.

Conflicts of interest

The authors declare no competing financial interest.

122 | *J. Mater. Chem. C*, 2024, **12**, 118–124

This journal is © The Royal Society of Chemistry 2024

Acknowledgements

References

1 J. Yang, K. Liu, X. Chen and D. Shen, *Prog. Quantum Electron.*, 2022, **83**, 100397–100425.

2 S. Surender, K. Prabakaran, S. Pradeep, I. D. Jacob, Y. F. Lu, S. Balakumar and K. Baskar, *Opt. Mater.*, 2023, **136**, 113462–113471.

3 W. Ruan and X. Meng, *ACS Appl. Nano Mater.*, 2023, 1019–1026.

4 S. Park, Y. Yoon, H. Kim, T. Park, K. Kim and J. Hong, *Nanomaterials*, 2023, **13**(5), 954–972.

5 B. Zhao, F. Wang, H. Chen, L. Zheng, L. Su, D. Zhao and X. Fang, *Adv. Funct. Mater.*, 2017, **27**(17), 1700264–1700271.

6 Z. Li, T. Yan and X. Fang, *Nat. Rev. Mater.*, 2023, **8**(9), 587–603.

7 Q. Cai, H. You, H. Guo, J. Wang, B. Liu, Z. Xie, D. Chen, H. Lu, Y. Zheng and R. Zhang, *Light: Sci. Appl.*, 2021, **10**(1), 94–124.

8 C. H. Kang, I. Dursun, G. Y. Liu, L. Sinatra, X. B. Sun, M. W. Kong, J. Pan, P. Maity, E. N. Ooi, T. K. Ng, O. F. Mohammed, O. M. Bakr and B. S. Ooi, *Light: Sci. Appl.*, 2019, **8**, 12–23.

9 X. Zhu, Y. Wu, G. Li, K. Zhang, S. Feng and W. Lu, *ACS Appl. Nano Mater.*, 2023, **6**(3), 2048–2062.

10 Q. Zhang, N. Li, T. Zhang, D. Dong, Y. Yang, Y. Wang, Z. Dong, J. Shen, T. Zhou, Y. Liang, W. Tang, Z. Wu, Y. Zhang and J. Hao, *Nat. Commun.*, 2023, **14**(1), 418–426.

11 C. Zhang, K. Liu, Q. Ai, X. Sun, X. Chen, J. Yang, Y. Zhu, Z. Cheng, B. Li, L. Liu and D. Shen, *Mater. Today Phys.*, 2023, **33**, 101034–101039.

12 J. Yue, X. Ji, S. Li, X. Qi, P. Li, Z. Wu and W. Tang, *Chin. Phys. B*, 2023, **32**(1), 016701–016706.

13 Y. Qin, H. Sun, S. Long, G. S. Tompa, T. Salagaj, H. Dong, Q. He, G. Jian, Q. Liu, H. Lv and M. Liu, *IEEE Electron Device Lett.*, 2019, **40**(9), 1475–1478.

14 X. Li, F. Xu, X. Wang, J. Luo, K. Ding, L. Ye, H. Li, Y. Xiong, P. Yu, C. Kong, L. Ye, H. Zhang and W. Li, *Phys. Status Solidi RRL*, 2023, 2200512–2200519.

15 J. Yue, X. Ji, X. Qi, S. Li, Z. Yan, Z. Liu, P. Li, Z. Wu, Y. Guo and W. Tang, *Vacuum*, 2022, **203**, 111270–111276.

16 Y. Yang, X. Y. Zhang, C. Wang, F. B. Ren, R. F. Zhu, C. H. Hsu, W. Y. Wu, D. S. Wuu, P. Gao, Y. J. Ruan, S. Y. Lien and W. Z. Zhu, *Nanomaterials*, 2022, **12**(9), 1510–1522.

17 C. Wu, F. Wu, H. Hu, S. Wang, A. Liu and D. Guo, *Mater. Today Phys.*, 2022, **28**, 100883–100904.

18 Z. Hu, Q. Cheng, T. Zhang, Y. Zhang, X. Tian, Y. Zhang, Q. Feng, W. Xing, J. Ning, C. Zhang, J. Zhang and Y. Hao, *J. Lumin.*, 2023, **255**, 119596–119602.

19 C. Zhang, K. Liu, Q. Ai, X. Huang, X. Chen, Y. Zhu, J. Yang, Z. Cheng, B. Li, L. Liu and D. Shen, *J. Phys. Chem. C*, 2022, **126**(51), 21839–21846.

20 R. Fornari, M. Pavesi, V. Montedoro, D. Klimm, F. Mezzadri, I. Cora, B. Pécz, F. Boschi, A. Parisini, A. Baraldi, C. Ferrari, E. Gombia and M. Bosi, *Acta Mater.*, 2017, **140**, 411–416.

21 A. Bosio, C. Borelli, A. Parisini, M. Pavesi, S. Vantaggio and R. Fornari, *ECS J. Solid State Sci. Technol.*, 2020, **9**(5), 055002–055007.

22 W. Chen, H. Luo, Z. Chen, Y. Pei, G. Wang and X. Lu, *Appl. Surf. Sci.*, 2022, **603**, 154440–154447.

23 W. Chen, Z. Chen, Z. Li, Z. Fei, Y. Pei, G. Wang and Z. He, *Appl. Surf. Sci.*, 2022, **581**, 152335–152343.

24 T. Zhang, Y. Li, Q. Cheng, Z. Hu, J. Ma, Y. Yao, C. Cui, Y. Zuo, Q. Feng, Y. Zhang, H. Zhou, J. Ning, C. Zhang, J. Zhang and Y. Hao, *Superlattices Microstruct.*, 2021, **159**, 107053–107060.

25 V. Montedoro, A. Torres, S. Dadgostar, J. Jimenez, M. Bosi, A. Parisini and R. Fornari, *J. Mater. Sci. Eng. B*, 2021, **264**, 114918–114924.

26 S. Li, J. Yue, C. Lu, Z. Yan, Z. Liu, P. Li, D. Guo, Z. Wu, Y. Guo and W. Tang, *Sci. China: Technol. Sci.*, 2022, **65**(3), 704–712.

27 Y. Ma, T. Chen, X. Zhang, W. Tang, B. Feng, Y. Hu, L. Zhang, X. Zhou, X. Wei, K. Xu, D. Mudiyanselage, H. Fu and B. Zhang, *ACS Appl. Mater. Interfaces*, 2022, **14**(30), 35194–35204.

28 Z.-Y. Yan, S. Li, Z. Liu, W.-J. Liu, F. Qiao, P.-G. Li, X. Tang, X.-H. Li, J.-Y. Yue, Y.-F. Guo and W.-H. Tang, *IEEE J. Sel. Top. Quantum Electron.*, 2022, **28**(2), 1–8.

29 Y. Qin, L. Li, X. Zhao, G. S. Tompa, H. Dong, G. Jian, Q. He, P. Tan, X. Hou, Z. Zhang, S. Yu, H. Sun, G. Xu, X. Miao, K. Xue, S. Long and M. Liu, *ACS Photonics*, 2020, **7**(3), 812–820.

30 S. Li, J. Yue, X. Ji, C. Lu, Z. Yan, P. Li, D. Guo, Z. Wu and W. Tang, *J. Mater. Chem. C*, 2021, **9**(16), 5437–5444.

31 Y. Li, D. Zhang, R. Lin, Z. Zhang, W. Zheng and F. Huang, *ACS Appl. Mater. Interfaces*, 2019, **11**(1), 1013–1020.

32 J. Jiang, J. Zhang and Z. Song, *J. Lumin.*, 2020, **221**, 117048–117052.

33 Z. Baji, I. Cora, Z. E. Horváth, E. Agócs and Z. Szabó, *J. Vac. Sci. Technol., A*, 2021, **39**(3), 032411–032419.

34 D. Wang, K. Ge, D. Meng and Z. Chen, *Mater. Lett.*, 2023, **330**, 133251–133254.

35 K. Yamamura, L. Zhu, C. P. Irvine, J. A. Scott, M. Singh, A. Jallandhra, V. Bansal, M. R. Phillips and C. Ton-That, *ACS Appl. Nano Mater.*, 2022, **5**(9), 12087–12094.

36 X. Sun, K. Liu, X. Chen, Q. Hou, Z. Cheng, J. Yang, Q. Ai, Y. Zhu, B. Li, L. Liu and D. Shen, *J. Mater. Chem. C*, 2023, **11**(9), 3227–3234.

37 D. Guo, X. Qin, M. Lv, H. Shi, Y. Su, G. Yao, S. Wang, C. Li, P. Li and W. Tang, *Electron. Mater. Lett.*, 2017, **13**(6), 483–488.

This journal is © The Royal Society of Chemistry 2024

J. Mater. Chem. C, 2024, **12**, 118–124 | 123

38 V. Vasanthi, M. Kottaisamy and V. Ramakrishnan, *Ceram. Int.*, 2019, **45**(2), 2079–2087.

39 T. Yamanaka, Y. Hayashi and H. Takizawa, *J. Ceram. Soc. Jpn.*, 2023, **131**(4), 100–105.

40 X. Cao, Y. Xing, J. Han, J. Li, T. He, X. Zhang, J. Zhao and B. Zhang, *Mater. Sci. Semicond. Process.*, 2021, **123**, 105532–105537.

41 Z. Liu, Y. Huang, C. Zhang, J. Wang, H. Li, Z. Wu, P. Li and W. Tang, *J. Phys. D: Appl. Phys.*, 2020, **53**(29), 295109–295114.

42 Y. Gao, X. Tian, Q. Feng, X. Lu, C. Zhang, J. Zhang and Y. Hao, *Ceram. Int.*, 2022, **48**(15), 22031–22038.

43 H. He, C. Wu, H. Hu, S. Wang, F. Zhang, D. Guo and F. Wu, *J. Phys. Chem. Lett.*, 2023, **14**(28), 6444–6450.

44 Y. Yang, H. Zhu, L. Wang, Y. Jiang, T. Wang, C. Liu, B. Li, W. Tang, Z. Wu, Z. Yang and D. Li, *Mater. Des.*, 2022, **221**, 110944–110949.

45 K. Wu, L. Zhou, C. Mao and Y. Chu, *Mater. Lett.*, 2023, **341**, 134161–134164.

46 H. Qian, X. Zhang, Y. Ma, L. Zhang, T. Chen, X. Wei, W. Tang, X. Zhou, B. Feng, Y. Fan, Y. Sun and B. Zhang, *Vacuum*, 2022, **200**, 111019–111026.

47 Y. Cheng, J. Ye, L. Lai, S. Fang and D. Guo, *Adv. Electron. Mater.*, 2023, **9**(4), 2201216–2201224.

48 Y. Cai, K. Zhang, Q. Feng, Y. Zuo, Z. Hu, Z. Feng, H. Zhou, X. Lu, C. Zhang, W. Tang, J. Zhang and Y. Hao, *Opt. Mater. Express*, 2018, **8**(11), 3506–3517.

49 Z. Liu, Y. Huang, H. Li, C. Zhang, W. Jiang, D. Guo, Z. Wu, P. Li and W. Tang, *Vacuum*, 2020, **177**, 109425–109429.

50 B. S. Qiao, Z. Z. Zhang, X. H. Xie, B. H. Li, X. Chen, H. F. Zhao, K. W. Liu, L. Liu and D. Z. Shen, *J. Mater. Chem. C*, 2021, **9**(11), 4039–4045.

51 G. Zeng, M.-R. Zhang, Y.-C. Chen, X.-X. Li, D.-B. Chen, C.-Y. Shi, X.-F. Zhao, N. Chen, T.-Y. Wang, D. W. Zhang and H.-L. Lu, *Mater. Today Phys.*, 2023, **33**, 101042–101049.

52 C. Xu, C. L. Senaratne, J. Kouvetakis and J. Menéndez, *Appl. Phys. Lett.*, 2014, **105**(23), 232103–232107.

53 X. Zou, D. Xie, Y. Sun and C. Wang, *Nano Res.*, 2022, 1–7.

124 | *J. Mater. Chem. C*, 2024, **12**, 118–124

This journal is © The Royal Society of Chemistry 2024